



HAL
open science

Operational Modal Analysis of hydroelectric turbines using an order based likelihood approach

Q. Dollon, J. Antoni, A. Tahan, M. Gagnon, C. Monette

► To cite this version:

Q. Dollon, J. Antoni, A. Tahan, M. Gagnon, C. Monette. Operational Modal Analysis of hydroelectric turbines using an order based likelihood approach. *Renewable Energy*, 2021, 165, pp.799-811. 10.1016/j.renene.2020.11.086 . hal-03211945

HAL Id: hal-03211945

<https://hal.science/hal-03211945>

Submitted on 15 Dec 2022

HAL is a multi-disciplinary open access archive for the deposit and dissemination of scientific research documents, whether they are published or not. The documents may come from teaching and research institutions in France or abroad, or from public or private research centers.

L'archive ouverte pluridisciplinaire **HAL**, est destinée au dépôt et à la diffusion de documents scientifiques de niveau recherche, publiés ou non, émanant des établissements d'enseignement et de recherche français ou étrangers, des laboratoires publics ou privés.



Distributed under a Creative Commons Attribution - NonCommercial 4.0 International License

Operational Modal Analysis of Hydroelectric Turbines Using an Order Based Likelihood Approach

Q. Dollon (a, b), J. Antoni (a), A. Tahan (b), M. Gagnon (c), C. Monette (d)

(a) Univ. Lyon, INSA-Lyon, Lab. Vibration Acoustique, F69621 Villeurbanne, France

(b) ÉTS, Montreal, Mechanical Engineering Department, H3C 1K3, Montreal, QC., Canada

(c) Institut de Recherche de Hydro-Québec (IREQ), J3X1S1, Varennes, QC., Canada

(d) Andritz Hydro Ltd., H9R 1B9, Pointe-Claire, QC. Canada

Contact : quentin.dollon.1@ens.etsmtl.ca

5483 3eme Av., H1Y 2W7 Qc, Montreal, Canada

Funding: Mitacs Acceleration, HydroQuebec, Andritz

About 5800 words. Figures 2, 8 and 9 must be printed with color.

Abstract - The purpose of this paper is to estimate hydroelectric turbine runner modal characteristics from experimental measurements coming from asynchronous regimes. This is achieved by investigating resonances generated by the interaction of a structural mode with harmonics of the rotating speed. Resonances are extracted using order tracking and processed with a Fast Bayesian algorithm in an ambient manner to estimate modal parameters and related uncertainties. Since data collection and effective processing of hydropower turbine field measurements is in its early stages, this paper lays some foundations in the treatment of transient regime measurements. A novelty in this approach lies in the use of a probabilistic identification tool in Order Based Modal Analysis (OBMA). A numerical experiment and a study from a hydroelectric Francis turbine field measurements are introduced to illustrate the method.

Keywords: Hydropower, Francis turbines, Structure Behavior, Ambient Modal Analysis, Fast-Bayesian Method.

List of symbols

i	Complex unit	ω_k	Discrete radial frequency $k \in \llbracket 1, N_f \rrbracket$
$p(x y)$	Probability of x given y	\mathbf{E}_k	$(m \times m)$ Excitation density matrix at ω_k (\mathbb{C})
\mathbf{I}	$(N_s \times N_s)$ Identity matrix	\mathbf{G}_k	$(N_s \times N_s)$ Response density matrix at ω_k (\mathbb{C})
$\hat{\mathbf{A}}$	Experimental estimation of \mathbf{A}	\mathbf{X}_k	$(N_s \times 1)$ Frequency response vector at ω_k (\mathbb{C})
$ \mathbf{A} $	Determinant of \mathbf{A}	\mathbf{A}_k	$(N_s \times N_s)$ Noise density matrix at ω_k (\mathbb{C})
\mathbf{A}^+	Moose-Penrose pseudo-inverse of \mathbf{A}	$D_k[\boldsymbol{\theta}]$	$(N_s \times 1)$ Amplification factor at ω_k (\mathbb{C})
\mathbf{A}^T	Transpose of \mathbf{A}	\mathbf{C}	$(4 + N_s \times 4 + N_s)$ Covariance matrix (\mathbb{R})
\mathbf{A}^*	Hermitian conjugate of \mathbf{A}	$\boldsymbol{\alpha}$	Tachometer record (angle vector)
\mathbf{x}^*	Interpolated vector of \mathbf{x}	$\boldsymbol{\varphi}$	$(N_s \times 1)$ Partial mode shape (\mathbb{C})
N_s	Number of investigated channels	ω_θ	Natural radial frequency
N_f	Number of frequency samples	ξ_θ	Damping ratio
$\boldsymbol{\theta}$	$(4 + N_s \times 1)$ SDoF parameter vector (\mathbb{C})	S_θ	Scaled PSD of modal force
$\mathcal{L}(\boldsymbol{\theta})$	Negative log-likelihood function (\mathbb{R})	Se_θ	Scaled PSD of channel noise

1. Introduction

A full grasp of turbine runner dynamic behavior is required in assessing the consequences of fatigue on life duration and crack propagation. Especially, an accurate determination of the actual behavior during transients is mandatory to determine the load levels [1, 2]. High amplitude stress cycles can lead to early damages and loss of reliability [3, 4]. Most of resonances observed in transient regimes emanate from the interaction between synchronous excitations coming from the harmonics of the

45 rotating speed, and a matching vibration mode of the turbine. Such phenomenon can generate periods
46 of intense vibration, possibly leading to extensive damages or even failure of the structure. The
47 prediction of structural modes allows defining optimal operating ranges in which resonances cannot
48 develop, and predicting the dynamic stress amplitudes the structure withstands during operations. In
49 some cases, operation during resonance may be allowed if excitation is sufficiently low and damping
50 sufficiently high, and a proper design is even more important in such situations to ensure safety.

51 In a foreseeable future, experimental measurements on turbine prototypes are expected to become
52 an integral part of this process [5, 6]. For both designers and users, experimental tools can be used for
53 validating and calibrating numerical models hence increasing structural reliability assessment
54 accuracy. Such approaches are particularly welcomed in the field of hydropower, as operational
55 conditions can strongly alter numerical predictions [7-9], and reduced model resonance studies cannot
56 be transposed to turbine prototypes [10]. The most practical way to achieve modal analysis for
57 operating devices is Operational Modal Analysis (OMA), where the structural behavior is investigated
58 without *prior* knowledge of the excitation, which is in effect the ambient excitation occurring during
59 operation. Experimental setup and cost are relatively low compared to other methods, so that OMA
60 has been widely developed since the early 1990's. Usually, only minor assumptions are needed to
61 characterize the response without knowing the excitation, but such analysis result in high uncertainties
62 to be evaluated.

63 Analysis of turbine operational modal characteristics is still restricted to a few studies [11-13], but
64 is gaining recognition with the demonstration of its benefits. Especially, it was shown that transient
65 events are particularly useful for detecting modal signatures [12, 13]. The purpose of this paper is to
66 present an OMA procedure tailored for hydroelectric turbines, capable of extracting modal
67 information and quantifying related uncertainties. The study focuses on asynchronous transient
68 regimes, in which the harmonics usually lead to resonances. System response is processed with a
69 Bayesian-based inference scheme which can return the modal statistical distributions with a low bias.

70 The paper is structured as follows. The first section introduces the main OMA tools available to
71 estimate modal parameters, and presents the concept of order based modal analysis. the ML Order
72 Based Modal Analysis (ML-OBMA) is presented in section 3, inspired by the works of S.-K. Au [14].
73 In section 4, several numerical cases are studied to test the algorithm. The model is finally
74 implemented on a hydroelectric case, where operational resonances during a coast-down are
75 characterized.

76 77 **2. Modal identification under random excitation**

78 OMA techniques are divided into four classes: they can process data in the time domain or in the
79 frequency domain, and can be parametric or non-parametric. Non-parametric algorithms perform
80 identification by splitting the signal into its modal contributions: see, e.g., Random Decrement
81 Technique (RDT) [15], Frequency Domain Decomposition (FDD) [16], Blind Source Separation (BSS)
82 [17]. Parametric approaches, for their part, attempt to fit Multi-Degree-of-Freedom (MDoF) model
83 parameters to experimental data. Time domain models are mostly based on signal autoregression or on
84 the output correlation matrix: auto-regressive (ARMA) [18], subspace methods (SSI) [19],
85 eigenrealization algorithm (ERA) or Ibrahim algorithm [20]. On the other hand, frequency domain
86 models are mainly based on density matrices: poly-reference Least-Square Complex Exponential (p-
87 LSCE) or polymax [21], frequency polyreference [20], maximum likelihood [22].

88 All these methods are deterministic and mostly rely on curve-fitting. Although ambient modal
89 analysis offers a wide range of identification tools, assessment of uncertainties is still limited to
90 specific procedures, and a general framework is yet to come. This is partly due to the many
91 uncertainty sources and their propagation: data acquisition, identification model, computation process,
92 etc. However, significant progress has recently been made in terms of taking stochastic uncertainties
93 into account [23]. The determination of modal parameter uncertainties is a first step in estimating the
94 uncertain vibrating response of structures [24]. Most time domain modal parameter variance models
95 are derived from the curve-fitting methods, using Monte Carlo algorithms or first-order developments.
96 Essentially, Taylor series are expanded to the first order derivative, for models such as SSI [25, 26] or
97 autoregressive [27]. In the frequency domain, statistical approaches mostly rely on Maximum
98 Likelihood Estimator (MLE). Such approach was combined with the polymax algorithm to reduce
99 noise and obtain distribution intervals, producing the Polymax Plus algorithm [28, 29]. Some accuracy
100 loss due to very noisy data were addressed more recently [30]. These algorithms are efficient modal

101 identifiers for long time-histories. MLE was finally extended into a Fast-Bayesian model through a
 102 Laplace approximation in 2017 [14]. MLE has many benefits as it is asymptotically unbiased and
 103 efficient (with respect to the Cramer-Rao lower bound) and convergent.

104 OMA models generally consider linear time-invariant systems, which results in the fundamental
 105 frequency input-output relation suggested in eq. (1). \mathbf{G}_k ($N_S \times N_S$), \mathbf{E}_k ($m \times m$) are respectively the
 106 discrete output and input spectral density matrices at radial frequency ω_k and \mathbf{H}_k ($m \times N_S$) is the
 107 frequency response function matrix containing the system characteristics. \mathbf{A}_k ($N_S \times N_S$) is the noise
 108 spectral density matrix. The equivalent time domain model can be obtained through the Wiener-
 109 Khinchin theorem. The objective is to determine \mathbf{H}_k for a given \mathbf{G}_k with \mathbf{E}_k unknown. This lack of
 110 knowledge is tackled by considering the ambient vibration as white noise having a constant power
 111 spectral density. Under this assumption, \mathbf{E}_k becomes a constant matrix, which is sufficient to estimate
 112 the poles of \mathbf{H}_k .

$$\mathbf{G}_k = \mathbf{H}_k^* \mathbf{E}_k \mathbf{H}_k^T + \mathbf{A}_k, \quad k \in \llbracket 1, N_f \rrbracket \quad (1)$$

113
 114 First introduced by K. Janssens et al. in 2006 [31], OBMA is a method combining advanced order
 115 tracking and an OMA algorithm to obtain modal characteristics. It has been extensively studied by
 116 E.D. Lorenzo [32, 33]. By considering hydroelectric turbines as multi-sine sweep generators
 117 (especially, the Rotor-Stator Interactions, RSI), resonances are easily extracted from the signal using
 118 Order Tracking (OT) methods. OT tools are capable of extracting the harmonic content of a mixed
 119 signal. Once synchronous resonances are extracted, excited modes are identified with OMA.
 120 Traditionally, the p-LSCE (or Polymax in its industrial name) identification algorithm is used [21].
 121 This parametric, deterministic frequency domain procedure is a poly-reference extension of the Least
 122 Square Complex Frequency algorithm (LSCF). It is a two-stage least square procedure that first
 123 identifies frequencies and damping ratios, and then identifies mode shapes based on stable poles. The
 124 processing of synchronous resonances with OMA is possible because the spectral density matrix of
 125 chirps in the order domain turns out to be constant, thus making it equivalent to an ‘order domain
 126 white noise’ (see, e.g., Figure 1). The analysis of chirp excitations, rather than stochastic excitations, is
 127 more representative of transient regimes. Especially, they provide more intense excitation forces, and
 128 resonances with higher Signal-to-Noise ratio (SNR).

129 In the current context, the p-LSCE has several limitations. First, the classical formulation of the
 130 problem does not consider uncertainties, which is crucial for treating poorly conditioned signals.
 131 Furthermore, its accuracy in presence of small data is shown limited in section 4, making the
 132 algorithm improper for short-time signal processing. For these reasons, the Fast-Bayesian approach is
 133 chosen to experimentally identify turbine modal characteristics. Indeed, this framework is well suited
 134 for such identifications. Typically, the identification is performed in the frequency domain, as required
 135 for an order-based formulation. Moreover, it is well adapted to process short series, since likelihood is
 136 effective for making inference with small data sample available, and will be shown robust against
 137 short-time estimation biases. Short-time estimations result in non-averaged spectra and excitation
 138 variance, that can make identification fail as the modal force is not perfectly constant.

139
 140

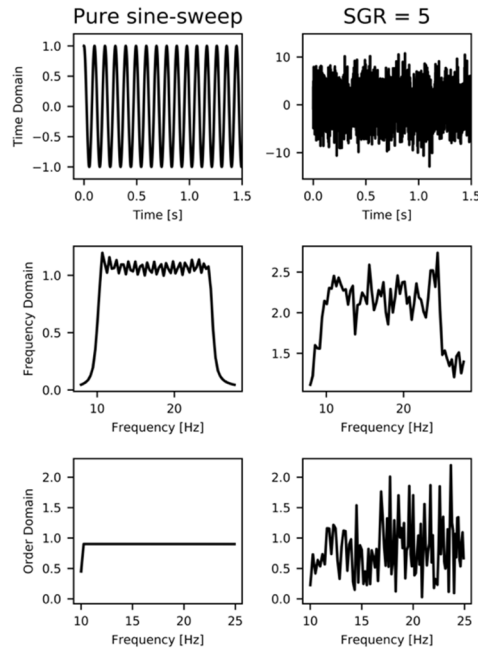


Figure 1: Time series, frequency content and order-tracked frequency response of a pure sine sweep and a harmonic signal buried in noise.

141
142
143

144

145 3. Bayesian order-based modal analysis

146 This section introduces a new OBMA formulation based on probabilistic modal analysis through
147 Bayesian inferences. Each subsection explains one step of the process, successively:

- 148 • The resonance detection.
- 149 • The angular domain order tracking.
- 150 • The identification scheme.

151

152 3.1. Resonance Detection

153 The data consists of an asynchronous time series containing N_s strain gauge measurement channels.
154 The first step is to map all synchronous resonance regions contained in the dataset. This is done by
155 investigating time-frequency spectra, using short-time discrete Fourier transforms. To ensure that the
156 observed amplification regions truly are resonances, a dual-channel Phase-Shift Analysis (PSA) might
157 be considered as it has been proven effective for diagnosis purposes [34, 35]. PSA examines the short-
158 time phase-shift diagram between two redundant sensors, as a complement to classical amplitude
159 spectrum studies. This is relevant because modal phase shifting between sensors is constant. Indeed,
160 rotational symmetric structure's modes are cylindrical or disk-like patterns, characterized by their
161 number of nodal diameters ν . Nodal diameters are diameters along which modal displacement is null,
162 thus separating isophase regions [36]. They can be positive or negative, the sign indicating the
163 direction of rotation: forward for $\nu > 0$, backward for $\nu < 0$. The motion along a mode has a constant
164 phase shift: between two consecutive blades separated by an angle of $\Delta\alpha = 2\pi/Z_b$, the phase-shift is
165 $\nu\Delta\alpha$. Then between N blades, the modal phase-shift is given by: $N\nu\Delta\alpha [2\pi]$, where $[\cdot]$ is the modulo
166 operator, ensuring a result on the trigonometric circle.
167

168 3.2. Angular Domain Order Tracking

169 In this study, Angular Domain (AD) Order Tracking is used because it does not need phase reference
170 and tackles the spectral leaking issue [32, 33]. A Computed Order Tracking (COT) algorithm is
171 performed to transform an asynchronous time series into a synchronous time series. This is based on a
172 two-stage interpolation as follows:

- 173 1. Determine the time-angle relation by integrating the rotational speed. This result in a relation
174 with constant Δt between each angular sample.
- 175 2. Interpolate this time-angle relation to obtain a new time reference with constant $\Delta\alpha$.

- 176 3. Interpolate the data with respect to the new time vector. The obtained data are synchronous, in
 177 the sense they are sampled at constant $\Delta\alpha$.
 178

179 Then, a non-windowed short-angle Fourier transform is performed on the resampled signal to exhibit
 180 its frequency content. For the sake of convenience, each interval corresponds to one runner revolution
 181 such that the spectrum resolution coincides with orders. An order spectrum is obtained for each
 182 studied revolution. Each line of the spectrum carries the amplitude of a synchronous harmonic in the
 183 signal, that are called orders. For each revolution, an exciting radial frequency ω_k is defined by
 184 averaging the harmonic frequency over the lap.

185 Bias in AD comes from the interpolation method and synchronous interval sampling. The
 186 interpolation bias is induced by the interpolating method, and residual shaft torsion vibrations that can
 187 induce tachometer signal fluctuations. This results in a slight shift of the angular signal. Concerning
 188 the synchronous interval splits, each interval must represent exactly one revolution, which is not
 189 necessarily the case: the angular shift between the first and the last point of the Fourier interval can be
 190 slightly different than 2π , and depends on the angular resampling rate. Most such errors are
 191 asymptotically unbiased, and can be reduced if the data are recorded with a very high sampling
 192 frequency as compared to the structure's natural frequencies. Also, the harmonic frequency averaging
 193 over a revolution involves a quasi-static assumption, reasonable for low accelerating systems only.
 194

195 3.3. SDoF Fast-Bayesian Inference

196 Hydroelectric runner modal frequencies are often close to each other, and might involve coupled-
 197 mode responses. However, harmonic excitations are well shaped to separate modes, since they can
 198 excite only some specific runner modes (see, for instance, the RSI theory presented in section 5). The
 199 use of a SDoF model is then advocated as it reduces the model complexity and related uncertainties.
 200 The bandwidth selection can be based on modal coherence techniques [37] or sensitivity to
 201 bandlimiting. The choice made here depends on the signal-to-noise ratio (SNR): Modal Assurance
 202 Criterion (MAC) should be preferred for high SNR, while sensitivity analysis is convenient for low
 203 SNR, since MAC becomes ineffective.

204 Once the SDoF assumption is assessed, the modal parameter vector estimate $\hat{\boldsymbol{\theta}}$ is determined
 205 using a Maximum Likelihood Estimator. This approach was initially developed in the early 2000's by
 206 Yuen [38]. A comprehensive state of the art is given in [22]. The underlying assumption is that the
 207 posterior probability is proportional to the likelihood, which is an unscaled version of the Baye's
 208 theorem with uniform priors. The experimental frequency data $\{\hat{\mathbf{X}}_k\}$ ($N_S \times 1$) is independent zero-
 209 mean complex Gaussian, and the likelihood function reads as:

$$210 \quad p(\{\hat{\mathbf{X}}_k\}|\boldsymbol{\theta}) = \prod_{k=1}^{N_f} \frac{\pi^{-N_s}}{|\mathbf{G}_k[\boldsymbol{\theta}]|} \exp[-\hat{\mathbf{X}}_k^* \mathbf{G}_k^{-1}[\boldsymbol{\theta}] \hat{\mathbf{X}}_k] \quad (2)$$

211 The likelihood is a function encapsulating the statistics of the data. For any parameter vector, it gives
 212 the conditional probability of observing the data given the physical model. $\mathbf{G}_k[\boldsymbol{\theta}] = \mathbb{E}\{\mathbf{X}_k \mathbf{X}_k^*\}$ is the
 213 theoretical density matrix. It derives from the resonance model given in eq. (3, 4), where $\boldsymbol{\theta} =$
 214 $(\omega_\theta, \xi_\theta, S_\theta, Se_\theta)^T$ is the modal parameter vector, including the natural radial frequency, the damping
 215 ratio, the modal excitation PSD and the noise PSD. The transition from eq. (1) to eq. (3) is reminded in
 216 Appendix A. $\boldsymbol{\varphi}$ ($N_S \times 1$) is the partial mode shape and $D_k[\boldsymbol{\theta}]$ the amplification factor for
 217 displacement data. \mathbf{I} ($N_S \times N_S$) is the identity matrix.

$$218 \quad \mathbf{G}_k[\boldsymbol{\theta}] = S_\theta D_k[\boldsymbol{\theta}] \boldsymbol{\varphi} \boldsymbol{\varphi}^T + Se_\theta \mathbf{I}_{N_s} \quad (3)$$

$$219 \quad D_k[\boldsymbol{\theta}] = \frac{1}{(\omega_\theta^2 - \omega_k^2)^2 - (2\xi_\theta \omega_\theta \omega_k)^2} \quad (4)$$

220 The main obstacle with the method is that the formulation given in eq. (2) is highly non-linear, and
 221 its maximization requires intensive and time-consuming computations. To reduce the complexity and
 222 some ill-conditioning problems, a modified version of the Negative Log-Likelihood Function (NLLF)
 223 was recently introduced [14, 39]. Based on an eigenvalue decomposition, this formulation allows to

224 express $\boldsymbol{\varphi}$ as a function of the other modes, reducing the optimization problem to the minimization of
 225 eq. (5), in which only 4 parameters need to be estimated. For typical data sizes, this process is fast, as
 226 the NLLF has a unique minimum in the parameter space [14].
 227

$$\begin{aligned} \mathcal{L}(\boldsymbol{\theta}) = & N_f N_s \ln(\pi) + \sum_{k=1}^{N_f} \ln(S_{\theta} D_k[\boldsymbol{\theta}] + S e_{\theta}) + (N_s - 1) N_f \ln(S e_{\theta}) \\ & + \frac{1}{S e_{\theta}} \left(\sum_{k=1}^{N_f} \hat{\mathbf{X}}_k^* \hat{\mathbf{X}}_k - \boldsymbol{\varphi}^T \mathbf{A}[\boldsymbol{\theta}] \boldsymbol{\varphi} \right) \end{aligned} \quad (5)$$

228

$$\mathbf{A}[\boldsymbol{\theta}] = \sum_{k=1}^{N_f} \left(1 + \frac{S e_{\theta}}{S_{\theta} D_k[\boldsymbol{\theta}]} \right)^{-1} \mathcal{R}e[\hat{\mathbf{X}}_k^* \hat{\mathbf{X}}_k] \quad (6)$$

229 A good Gaussian approximation of the posterior densities relies on a second-order Taylor
 230 expansion of the NLLF. Since such computation requires intensive efforts, posterior distributions are
 231 approximated with the Laplace method, i.e., with normal distributions centered at the MPV with
 232 standard deviations deduced from the covariance matrix $\hat{\mathbf{C}}$, obtained with eq. (7). This gives the Fast-
 233 Bayesian method which leads to conditional distributions, but is faster, and any loss of accuracy it
 234 provides as compared to the unconditional distribution are considered insignificant [14]. In other
 235 terms, the likelihood around the MPV is assumed Gaussian and independent, which is apparently
 236 reasonable for large data processing.
 237

$$\hat{\mathbf{C}} = (\nabla \mathbf{v}_c)(\hat{\boldsymbol{\theta}}) \cdot [\nabla^2 \mathcal{L}(\hat{\boldsymbol{\theta}})]^{\dagger} \cdot (\nabla \mathbf{v}_c)^T(\hat{\boldsymbol{\theta}}) \quad (7)$$

$$\mathbf{v}_c(\hat{\boldsymbol{\theta}}) = \left(\hat{\boldsymbol{\theta}}, \frac{\hat{\boldsymbol{\varphi}}}{\|\hat{\boldsymbol{\varphi}}\|} \right) \quad (8)$$

238

239 In eq. (7), $\hat{\mathbf{C}}$ is obtained as the inverse of the NLLF Hessian at the MPV, through a constraint
 240 function that takes into account the mode shape normalization, denoted \mathbf{v}_c and expressed in eq. (8).
 241 The solution is a "pseudo-inverse" computation in the sense it ignores the null eigenvalues arising
 242 from the constraint singularities.
 243

244

4. Numerical Testing

245

246

247

248

249

250

251

252

253

254

4.1. Illustrative computational example

255

256

257

258

259

260

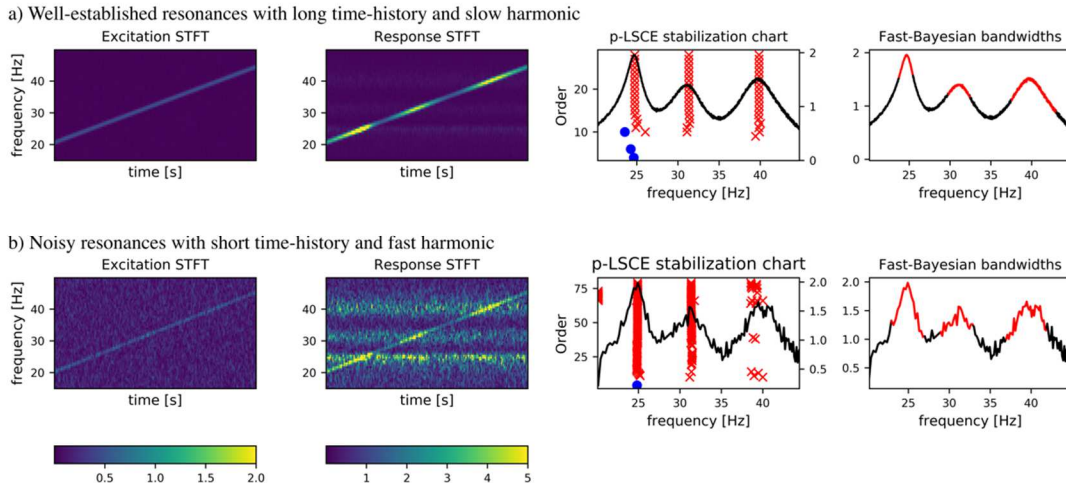
261

262

263

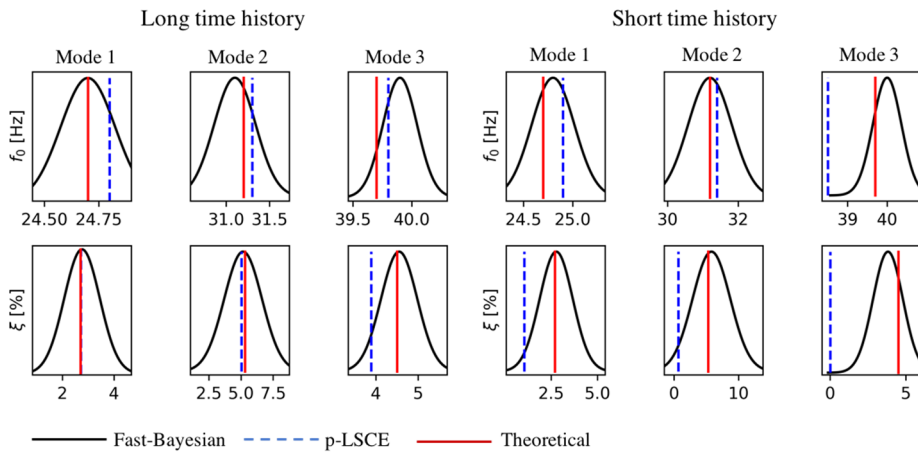
The model is now used on a simulation example, and compared to the p-LSCE. Let consider a 3-DoF
 system with known modal properties, and $N_s = 10$ measured DOF. Three modes are expected at
 24.7Hz, 31.2Hz and 39.7Hz, with damping ratios 2.7%, 5.3% and 4.5%, respectively. The system is
 first computed in the time domain using a state-space model. The sampling frequency is 2.5kHz,
 making the OT biases insignificant. The AD resampling is 2,500 samples per revolution. Two
 simulations are performed. On the first hand, the system is excited with a pure and low sine-sweep,
 capturing a well-shaped response. On the other hand, the system is excited by a mix of a sine-sweep
 and a stochastic source, which embodies the non-flat excitation behavior. The scanning harmonic is
 faster, delivering short-time spectra and ill-conditioned responses. The two simulations are presented

264 in Figure 2a. and b. left, depicting the excitation input and response output time-frequency
 265 distributions. The responses are extracted using OT, and processed with the p-LSCE and with the Fast-
 266 Bayesian inference. The p-LSCE stabilization diagram and the Fast Bayesian bandwidth selection are
 267 presented on the right side of Figure 2. The p-LSCE converges fast for the well-shaped responses, and
 268 the three modes are stable from order 15. Notice that the stabilization diagrams are very clear and easy
 269 to interpret, since the spurious modes are computed with negative damping. However, the p-LSCE
 270 seems inadequate for processing ill-conditioned responses: the first and second modes are identified at
 271 low orders, but the third mode is very unstable, and the algorithm hardly identifies a stable pole
 272 around order 70. A stable spurious mode is present around 20Hz, between order 65 and 75. The Fast-
 273 Bayesian bandlimited inputs are obtained using the MAC criterion for the first simulation, and using a
 274 sensitivity analysis for the second simulation.
 275



276
 277 **Figure 2:** 3-DOF system response. a) well-shaped responses. b) ill-conditioned responses.

278 The identification results are presented in Figure 3. When dealing with long time histories, the two
 279 approaches are consistent and identified modal parameters are close to the theoretical values. The
 280 Bayesian approach provides estimates with low uncertainties. The short time history case is properly
 281 identified by the Fast-Bayesian scheme, but the related uncertainties are very large, especially for the
 282 damping estimates. The p-LSCE finds accurate natural frequencies for modes 1 and 2, but fails at
 283 properly identifying the third natural frequency. The damping ratios are systematically under-
 284 estimated, and the identified modes 2 and 3 are almost undamped.
 285



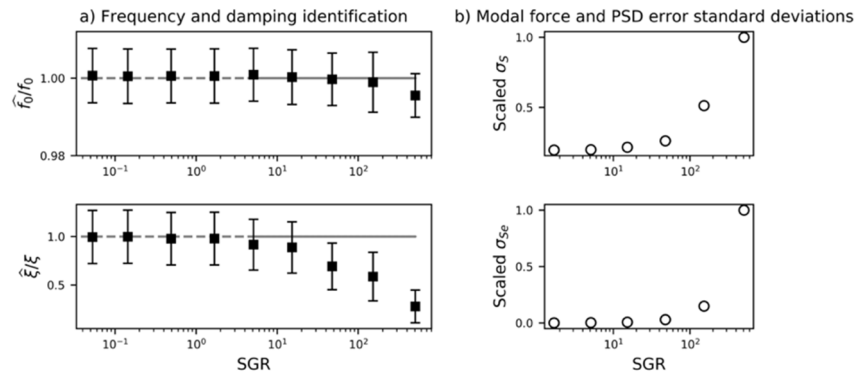
286
 287 **Figure 3:** p-LSCE and Fast-Bayesian identification.

288 The processing of short-time spectra cannot be handled correctly with the p-LSCE. The stabilization
 289 diagram indicates over-fitting at high order that can be sufficient for capturing stable poles, but the
 290 results show that the damping ratios are not representative of the studied dynamical modes.
 291 Conversely, the Fast-Bayesian is a legitimate algorithm that can be used to study short-time responses.

292 As demonstrated in this section, the identification is still accurate with sparse data and the error
 293 between the MPV and the theoretical values is low. Nevertheless, the computed uncertainties grow
 294 when the data becomes limited. Although this is naturally expected, the posterior deviation can be
 295 wide and not representative of the real parameter variability. Consequently, these uncertainties can
 296 make the experimental characterization unusable in an industrial context.

298 4.2. Robustness against non-flat excitation spectra

299 Once the algorithm is shown adequate for processing short-time histories, it is necessary to assess in
 300 which extent the identification remains acceptable. For this, it is proposed to test the ML-OBMA on a
 301 linear sine sweep excitation passing through a resonance, with different levels of deviation from a
 302 constant excitation force. To be consistent with experimental data, a set of $N_s = 10$ channels with
 303 equally distributed mode shape ratios is considered. An ML-OBMA was performed on several
 304 datasets with different variance intensity levels. The variable control is the Stochastic Gain Ratio
 305 (SGR), defined as the power ratio of the white noise deviations (the ‘stochastic’ part) and the averaged
 306 white noise. The FM rate was set to $6 \cdot 10^{-2} \text{ Hz/s}$, and the modal frequency and damping are 50Hz
 307 and 2.5%. Figure 4.a presents the sensitivity results. The markers draw the normalized most probable
 308 value (scaled on the theoretical value), and the bars represent ± 3 normalized standard deviations.
 309



310 **Figure 4:** a) Modal parameter most probable values as a function of SGR. Uncertainty bars cover 3 c.v.
 311 b) Modal force and PSD error standard deviations. The two distribution parameters evolve jointly and
 312 tend to when the noise intensity is too high.
 313

314 It is observed that even for noise with a high SGR (near 500), the theoretical natural frequency still
 315 lies within a 95% credibility interval. When the stochastic gain ratio is lower than 100, the error
 316 between f_0 and \hat{f}_0 drops below 1%. The damping ratio’s MPV only converges toward the theoretical
 317 value for very low SGR, and tends to be underestimated for SGR greater than 20. This is explained by
 318 the modal force PSD standard deviation discrepancy, as shown in Figure 4.b. The underestimation of
 319 the damping ratio while the excitation variance is too high is in keeping with the well-known damping
 320 underestimation in OMA. The damping and radial frequency variance seem relatively insensitive to
 321 the stochastic excitation amplitude. This is because the modal force PSD and noise PSD uncertainties
 322 increase drastically with the SGR, dominating the other modal parameter variabilities. The MPVs are
 323 not displayed, but the noise PSD increases linearly with SGR, i.e., the model equates a fraction of
 324 stochastic excitation with channel noise. On the other hand, the modal force PSD decreases to
 325 conserve signal power, and is reduced by 50% for a SGR of 100.

326 The model appears to be robust against stochastic excitation processes, which is an important
 327 factor for ambient measurement processing. The identification fails as soon as the modal force PSD
 328 and noise PSD standard deviations begin to diverge. The SGR at which these deviations diverge is a
 329 function of the number of channels, the higher the number of channels the lower the critical SGR.
 330

331 4.3. Sensitivity to the frequency modulation rate

332 Two aspects of the sine sweep excitation frequency modulation rate need to be considered. The first
 333 deals with model uncertainties, while the second undermines the structure of the non-stationary natural
 334 response. With a low frequency-modulated excitation τ , uncertainties appear to be low and MPVs are
 335 well estimated. When the FM rate increases, uncertainties seem to increase linearly with it, as shown
 336 in Figure 5: when τ increases, resonances develop and vanish faster. This shrinks the time duration of

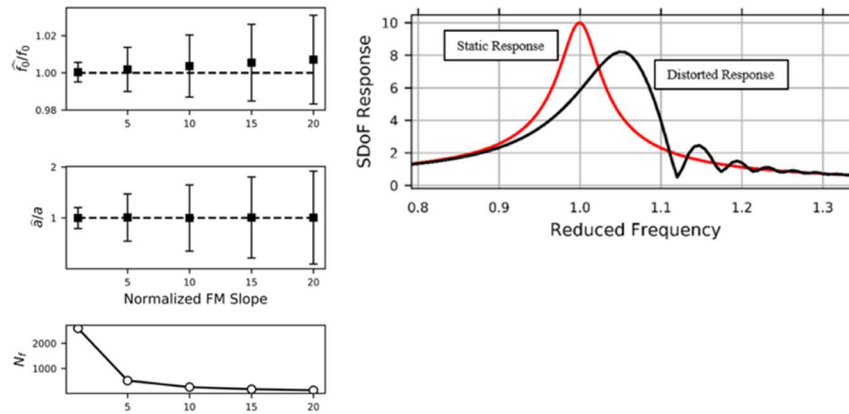
337 the signal, as shown in the lower part of Figure 5 (N_f decreases as the time duration decreases). The
 338 model accuracy is inevitably reduced because fewer observations are available. This remark is known
 339 as noise mitigation process. Damping estimations remain good, but the frequency MPV tends to be
 340 overestimated during the run-up (and underestimated during run-downs), the steeper the slope the
 341 higher the error.

342 For higher FM slopes, another issue may arise due to dynamic distortions of the classical steady-
 343 state response. These are due to the inability of the system to instantaneously match the excitation.
 344 Such distortions have been widely investigated for electronics, and more recently, in the field of
 345 mechanical engineering [40]. The ISO-7626 standard defines some criteria under which the response
 346 distortion is low enough to be neglected. For example, the condition for linear FM excitation is $h \times$
 347 $\tau_{\max} < 3.6 (f_0 \xi)^2$ [Hz/s]. When these conditions are not fulfilled, the response may be distorted and
 348 cannot be modelled with a static transfer function. Figure 5 (right side) demonstrates an example of
 349 such a distorted response: epistemic uncertainties can be encountered when dealing with out-of-
 350 standard systems, and natural frequencies deviate from their original value. At the same time, damping
 351 ratios are unpredictable if distortions are not modelled properly.

352 Dynamic distortions can also play a role in the uncertainty rise seen in Figure 5 (left), as it
 353 introduces

354 a modeling error leading to the expansion of credibility intervals. Identification in the presence of such
 355 dynamic behaviors was not considered in this paper, but authors seemed to deem it worthwhile to
 356 mention its existence and potential effects on parameter identification.

357
 358



359 **Figure 5:** Left – Uncertainties increasing with FM slope. Right – The dynamic distortion
 360 of modal response when subjected to strong frequency modulated excitations.
 361

362

363 5. Case study: an experimental analysis of a Francis turbine during coast-down

364 5.1. Turbine characteristics and experimental setup

365 The case study is based on a vertical medium head Francis hydroelectric turbine. It is part of a run-of-
 366 the-river plant located in Quebec, Canada. The turbine has a specific speed of $n_Q = 57$, and a
 367 synchronous speed of 163.6 RPM. The flow in the penstock is directed into a spiral casing, and fed
 368 into the runner through a distributor of $Z_g = 20$ guide vanes. The runner is a Francis runner of
 369 diameter 4.4m and height 2.7m, and is composed of $Z_b = 13$ blades. For this kind of geometry, 7
 370 cylindrical mode shapes are expected. Such patterns are cyclic-symmetric with nodal diameters $|\nu|$
 371 between 0 and 6.

372 In many medium-to-high head hydraulic turbines, the main harmonics of the rotating speed are
 373 the Rotor-Stator Interactions (RSI) [41]. The RSI theory can be jointly used with Phase-Shift Analysis
 374 to determine the mode shapes. Indeed, RSI pressure waves have specific and predictable patterns and
 375 frequency, which will perform a selective excitation that only excite matching mode shapes.
 376 Typically, the RSI seen from the runner generate excitations at the wicket gate passing frequencies:
 377 $f_{RSI}^n = nZ_g f_0$. The RSI is capable of exciting modes with $\nu = mZ_b - nZ_g$ nodal diameters on the
 378 runner. Table 1 summarizes the runner RSI properties, that will be used latter when identifying the
 379 mode shapes. The phase-shift is calculated using section 3.1.

Table 1: RSI characteristics in the runner rotating coordinate system.

RSI harmonic n	Frequency f_{RSI}^n	Excitation shape ν	Expected phase- shift [rad]
1	$20 f_0$	6	-0.97
2	$40 f_0$	-1	-1.93
3	$60 f_0$	5	-2.90
4	$80 f_0$	-2	2.42

381

382

383

384

385

386

387

388

389

Data were recorded during an asynchronous coast-down transient experiment in no-load conditions. Two blades separated by an angle of 111° were instrumented with strain gauges, as presented in Figure 6.a. The blade intrados were instrumented with three strain gauge rosettes located in the band junction to a blade leading edge and trailing edge, and in the middle crown-blade weld, as shown in Figure 6.b. The blade extrados were instrumented with two uniaxial gauges, one close to the crown, and the other close to the band. The locations were the same from one blade to the other. This enables the turbine runner mode shapes to be determined through a phase-shift analysis. The rosette and uniaxial gauges were oriented in agreement with the expected principal strain sensor.

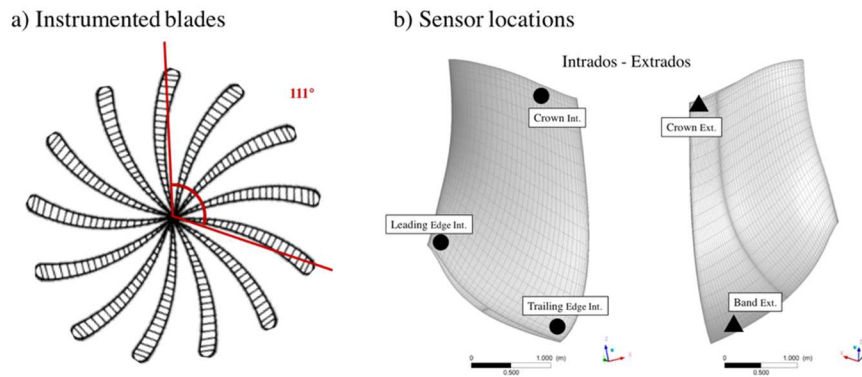


Figure 6: a) Instrumented blades. The two blades are separated by an angle of 111° .
b) Strain gauge location on the instrumented blades. Circles represent rosette gauges, triangles, uni-axial gauges.

390

391

392

393

394

395

5.2. Mode Shape Identification

396

397

398

399

400

The analysis of experimental amplitude and phase-shift spectra between redundant sensors was conducted first. Examples of time-frequency distributions are shown in Figure 7, as related to the crown extrados. Phase-shift spectra are amplitude-filtered and show only phases associated with a high enough amplitude. With a long enough Fourier windowing, amplitude spectra show five operating deflection shapes (ODS).

401

402

403

404

405

406

407

408

The ODS of interest are those triggered by synchronous harmonics. It should be recalled that a harmonic interaction requires both a matching frequency and a compatible nodal diameter. As expected by the RSI theory, a ND5 is excited by the 60-th harmonic around 60Hz when the rotating speed is around 1Hz (see Table 2). A ND0 is excited by the 13-th harmonic with a zero phase-shift. This correspond to the Blade Passing Frequency seen from the stationary cascade. Such frequency can be excited either by by an improper flow distribution, a local default on the structure or a casing asymmetry. Then, the ND0 can be excited every time a blade passes through the pressure fluctuation, i.e. 13 times per revolution.

409

410

411

412

413

414

415

416

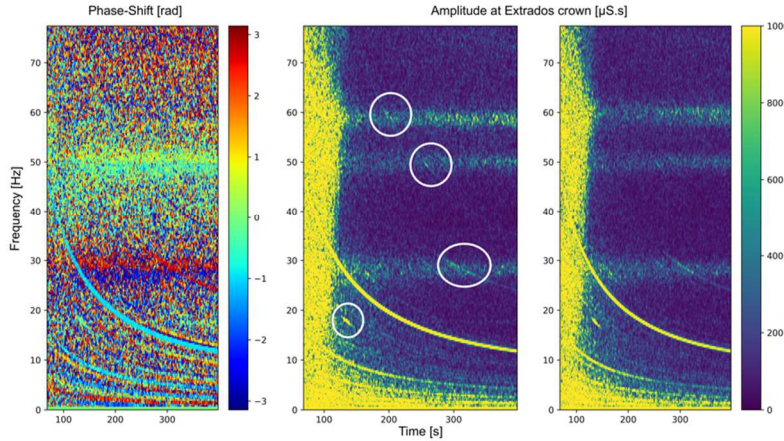
417

In the studied turbine, the authors were surprised to find out that some resonances are not induced by the RSI harmonics, but by harmonics in their vicinity. As shown in Figure 8, two resonances are induced by the 41-th and 62-nd harmonics while the RSI theory predicts excitations with the 40-th and 60-th harmonics. While excited mode shape nodal diameters should be ND-1 and ND5, the observed phase-shift indicates that the excited nodal diameters are respectively ND-2 and ND3, as reported in Table 2. Without going further in details, these observations are the result of a stationary point force excitation. Readers should refer to the works of Wildheim for deeper explanations [42].

Table 2: Excitation shape and frequency domain of the identified resonances.

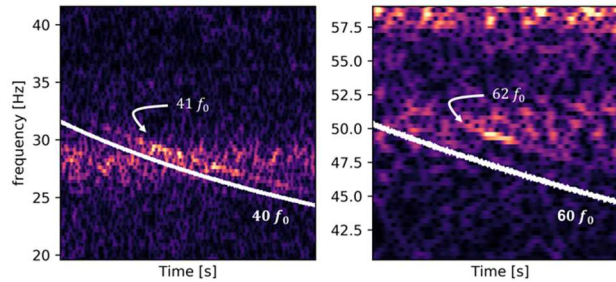
Resonance Band	Rotating speed [Hz]	Phase-shift [rad]	Mode shape nodal diameters $ v $
[15, 20] Hz	1.3	0	0
[20, 40] Hz	0.7	2.42	-2
[40, 50] Hz	0.8	-0.48	3
[50, 60] Hz	1.0	-2.90	5

418
419



420
421
422
423

Figure 7: ODS analysis of principal direction of extrados crown Rosette gauge. On the left, phase-shift spectrum of the redundant gauges. On the right, redundant amplitude spectra.



424
425

Figure 8: Unexpected resonances with the 41-th and 62-nd harmonics.

426

5.3. Modal identification using ML-OBMA

427

428

429

430

431

432

433

434

435

436

437

438

439

Each resonance is processed with an ML-OBMA to extract both frequency and damping distributions. Bandwidth were selected using a MAC analysis for the ND0, while ND-2, 3 and 5 were bandlimited using a sensitivity analysis. An example of such an analysis for ND3 is provided in Figure 9. A band of $\Delta f = 8Hz$ is chosen as modal parameters stable and uncertainties low. Identification results are presented in Figure 10. Two types of result were investigated: a direct ML-OBMA inference as described in the previous sections and the distributions after taking into account short-time noise variance through Markov chains. 10^3 process realizations were needed to ensure a good statistical convergence. Results show that the sole likelihood inference provides robust and accurate uncertainty bounds while Markov chains do not bring any significant change. This means that the Fast-Bayesian is not sensitive to non-flat noise PSD.

440
441

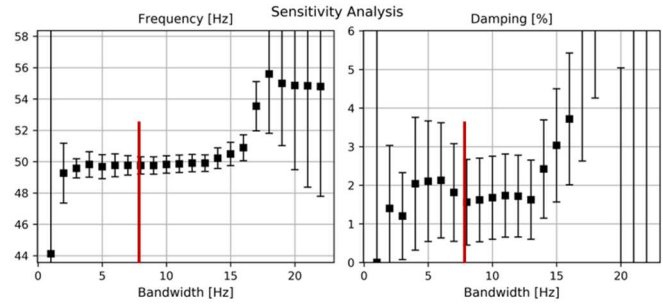


Figure 9: ND3 bandlimiting using a sensitivity analysis.

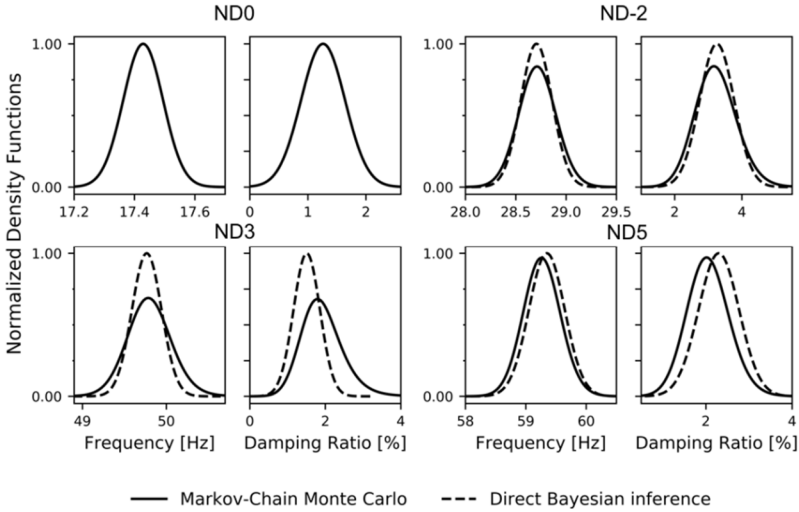


Figure 10: Frequency and damping distributions after ML-OBMA and after Markov chains ML-OBMA.

442
443
444

445 ND0 distributions remain unchanged after experimental uncertainties are calculated. This is
446 explained by the high quality of the signal, which causes the noise to have almost no impact.
447 Frequency distributions are narrow distributions, almost Gaussian with small standard deviations,
448 while damping distributions seem skewed, developing a wider tail for upper damping values. This is
449 particularly observable for ND3. A high uncertainty exists for damping estimation, much like with
450 many modal analysis extraction tools. Table 3 presents the parameter statistical distributions. The most
451 probable values (MPV) and coefficients of variation (ratio of standard deviations over MPVs) are
452 drawn.

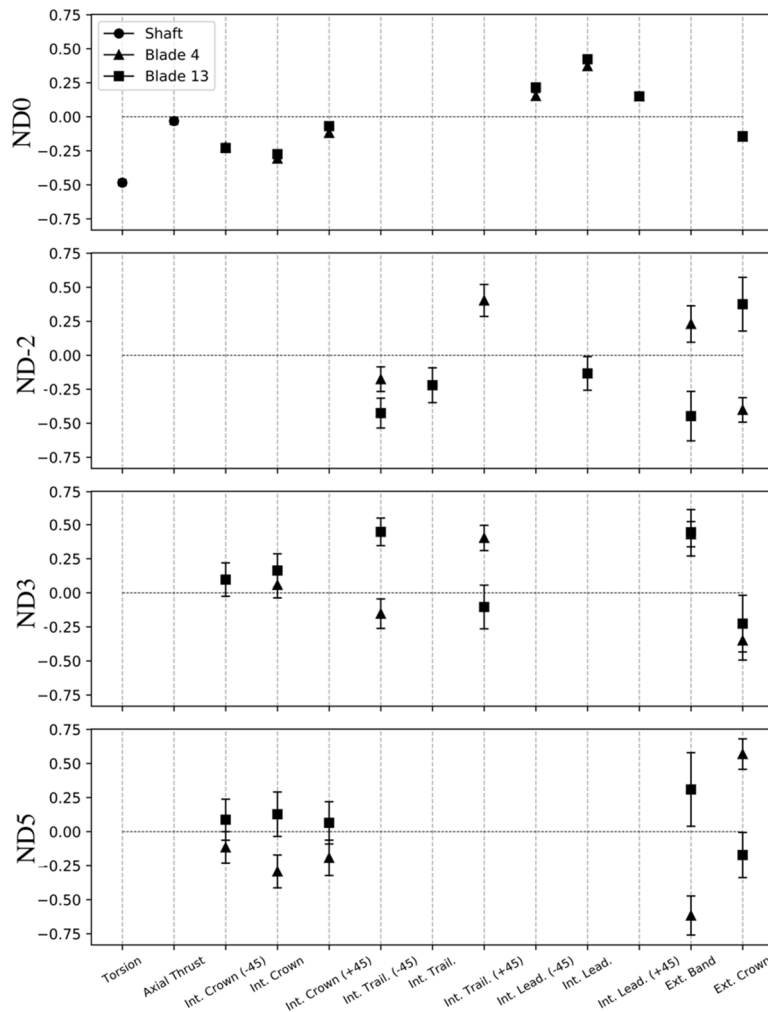
453 The deviation of the estimated mode shape from the real mode shape can be estimated, without the
454 latter being known. This is done using a stochastic representation of the mode shape: $\boldsymbol{\varphi} =$
455 $\boldsymbol{\varphi} \|\boldsymbol{\varphi}\|^{-1}$, $\boldsymbol{\varphi} \sim \mathcal{N}(\hat{\boldsymbol{\varphi}}, \hat{\mathbf{C}}_{\boldsymbol{\varphi}})$, and using an eigen-representation of the MAC. For more details please refer
456 to [14]. ML-OBMA provides very close estimations of mode shapes, since the modal assurance
457 criterion is high with a low c.v. As shown in Figure 11, the MAC may be close to 1, mode shape can
458 strongly deviate from the expected target (ND5), or slightly (ND0). The MAC value does not reflect
459 this inaccuracy. The MAC c.v. gives the global degree of adequacy, accounting for the norm
460 constraint $\|\boldsymbol{\varphi}\| = 1$. This degree of uncertainty depends on the SNR, the higher the SNR, the lower
461 the error: ND0 has an SNR of 7.4dB and a MAC c.v. of 2.7%, while ND5 has an SNR of 0.95dB with
462 a MAC c.v. of 7.7%.

463
464
465
466
467
468
469
470

471
472
473
474
475
476
477
478
479
480
481
482
483
484
485

Table 3: Modal parameter distributions for identified modes.

	M.P.V. (SI)	C.V.	M.P.V. (SI)	C.V.
	ND0		ND3	
Frequency [Hz]	17.43	3.8×10^{-3}	49.79	5.2×10^{-3}
Damping ratio [%]	1.26	3.0×10^{-1}	1.39	5.4×10^{-1}
Excitation PSD	2.2×10^6	1.6×10^{-3}	1.2×10^6	7.3×10^{-5}
[μS]				
Noise PSD [$\mu S/Hz$]	1.7×10^{-2}	2.6×10^{-4}	7.6×10^{-4}	1.4×10^{-5}
Shape (MAC)	0.999	2.7×10^{-2}	0.999	4.5×10^{-2}
	ND-2		ND5	
Frequency	28.72	6.4×10^{-3}	59.25	5.2×10^{-3}
Damping ratio	2.75	2.8×10^{-1}	2.01	2.4×10^{-1}
Excitation PSD	3.3×10^5	9.2×10^{-5}	4.3×10^6	7.8×10^{-5}
Noise PSD	1.2×10^{-3}	1.6×10^{-5}	2.0×10^{-3}	5.9×10^{-6}
Shape (MAC)	0.999	5.4×10^{-2}	0.997	7.7×10^{-2}



486
487
488

Figure 11: Mode shapes for identified modes.

489
490
491
492
493
494
495
496

5.4. Comparison with numerical simulations

Once the experimental frequencies are characterized, it is possible to use them to validate the numerical predictions. In order to compare the experimental results to the numerical computations, several simulations were performed to obtain the runner modal analysis in different configurations. As it is well known that the modal behavior of a turbine is strongly influenced by the surrounding water, the fluid-structure interaction (FSI) added mass effect must be considered in the simulations when computing the natural frequencies. The full runner geometry is considered, and the meshing for one

497 blade is presented in Figure 12, with tetrahedral elements. The shaft is not included in the simulation,
 498 which could have a significant influence on the prediction of nodal diameters 0 and 1. Instead, a zero-
 499 motion boundary condition is imposed at the shaft coupling ring.
 500 The FSI are treated like a structural-acoustical problem in Ansys. Three different water volumes were
 501 modelled, as shown in Figure 13. In the first simulation, a large volume of water is studied with a fluid
 502 domain of 0.5m around the runner. In the second simulation, a restricted volume of water is used with
 503 0.1m distance between water external boundary and runner largest diameter, to take into account the
 504 runner confinement effect. In the third simulation, a more realistic geometry with a larger fluid domain
 505 is considered, including the upper and lower labyrinths real gaps (1-2mm), a portion of the distributor
 506 inflow, and the upper part of the draft tube. Obtained fluid volumes are meshed using quadratic
 507 elements with approximately 2M nodes. The external fluid bounds are treated as reflective walls. In
 508 the simulations, the system is considered undamped and no damping prediction is available. For this
 509 reason, the comparison with the experimental results is restricted to the natural frequencies.
 510
 511



512
 513 **Figure 12:** Turbine mesh for one blade.

512
 513

514
 515



516
 517 **Figure 13:** FEM analysis for the simulations with acoustic fluid.

516
 517

518
 519 Table 4 presents the relative error between the identified frequencies and the numerical computations.
 520 The ND0 is a torsion mode, which is strongly influenced by the shaft. Since the finite element model
 521 did not include the shaft, the large overestimation of the modal analysis is easily explainable.
 522 Theoretically, nodal diameters larger than 2 are fully balanced over the runner and they should not be
 523 influenced by the shaft. Consequently, the modal prediction is very close to the experimental
 524 observations. From simulation 1 to 2, the error decreases by 10% for modes 2 and 3. The best results
 525 are naturally obtained from the complex fluid domain geometry used in simulation 3, with a remaining
 526 error of about 1%. This is mainly due to the confinement effect, which is known to reduce the natural
 527 frequencies.

528 Although experimental identification is incomplete and misses several modes, available results can
 529 be used to calibrate models and obtain more precise load levels throughout the turbine. This
 530 calibration will also have impact on non identified modes, what will result in an improvement of stress
 531 predictions, then turbine fatigue and structural health.
 532

Table 4: Comparison of experimental and numerical natural frequencies of identified modes.

Mode shape nodal diameters $ v $	Experimental freq. [Hz]	Simulation 1	Simulation 2	Simulation 3
0	17.43	232%	211%	180%
2	28.72	36%	22%	-2%
3	49.79	16%	9%	1%
5	59.25	3%	0.5%	-0.5%

534

535

536

6. Conclusion

537

538

539

540

541

542

543

544

545

546

547

548

549

550

551

552

553

554

555

556

557

558

559

560

561

562

563

7. Acknowledgement

564

565

566

8. References

- [1] Presas A, Luo Y, Wang Z and Guo B 2019, Fatigue life estimation of Francis turbines based on experimental strain measurements: Review of the actual data and future trends, *Renewable and Sustainable Energy Reviews* **102** 323-29 (DOI 10.1016/j.rser.2018.12.001)
- [2] Kougias I, Aggidis G, Avellan F, Deniz S, Lundin U, Moro A, Muntean S, Novara D, Pérez-Díaz J-I, Quaranta E, Schild P and Theodossiou N 2019, Analysis of emerging technologies in the hydropower sector, *Renewable and Sustainable Energy Reviews* **113** (DOI 10.1016/j.rser.2019.109257)
- [3] Gagnon M, Tahan A, Bocher P and Thibault D 2010, Impact of startup scheme on Francis runner life expectancy, *IOP Conf. Ser.: Earth Environ. Sci.* **12** (DOI 10.1088/1755-1315/12/1/012107)
- [4] Goyal R and Gandhi B-K 2018, Review of hydrodynamics instabilities in Francis turbine during off design and transient operations, *Renewable Energy* **116** (DOI 10.1016/j.renene.2017.10.012)
- [5] Gagnon M, Tahan A, Bocher P and Thibault D 2014, Influence of load spectrum assumptions on the expected reliability of hydroelectric turbines: A case study, *Structural Safety* **50** 1-8 (DOI 10.1016/j.strusafe.2014.03.008)
- [6] Liu X, Luo Y and Wang Z 2016, A review on fatigue damage mechanism in hydro turbines, *Renewable and Sustainable Energy Reviews* **54** 1-14 (DOI 10.1016/j.rser.2015.09.025)

- [7] Valentin D, Ramos D, Bossio M, Presas A, Egusquiza E and Valero C 2016, Influence of the boundary conditions on the natural frequencies of a Francis turbine, *IOP Conf. Ser.: Earth Environ. Sci.* **49** (DOI 10.1088/1755-1315/49/7/072004)
- [8] Trivedi C and Cervantes M-J 2017, Fluid-structure interactions in Francis turbines: A perspective review, *Renewable and Sustainable Energy Reviews* **68** 87-101 (DOI 10.1016/j.rser.2016.09.121)
- [9] Liu X, Luo Y, Presas A, Wang Z and Zhou L 2018, Cavitation Effects on the Structural Resonance of Hydraulic Turbines: Failure Analysis in a Real Francis Turbine Runner, *Energy* **11** (DOI 10.3390/en11092320)
- [10] Valentin D, Presas A, Valero C, Egusquiza M, Egusquiza E, Gomes J and Avellan F 2020, Transposition of the mechanical behavior from model to prototype of Francis turbines, *Renewable Energy* (DOI: doi.org/10.1016/j.renene.2020.01.115)
- [11] Gagnon M, Tahan A, Coutu A and Thomas M 2006, Operational Modal Analysis in presence of harmonic excitations: case study on hydroelectric turbine components, *Canadian Vib. Association* (ISBN 2-921145-61-8)
- [12] Valentin D, Presas A, Bossio M, Egusquiza M, Egusquiza E and Valero C 2018, Feasibility of Detecting Natural Frequencies of Hydraulic Turbines While in Operation, Using Strain Gauges, *Sensors* **18** (DOI 10.3390/s18010174)
- [13] Dollon Q, Tahan A, Antoni J, Gagnon M and Monette C 2019, Dynamic Characterization Of Hydroelectric Turbine In Transient Using OBMA And Phase-Shift Analysis, *Surveillance Vishno Conf.* (HAL 02190260)
- [14] Au S-K 2017, Operational Modal Analysis, Modeling, Bayesian Inference, Uncertainty laws, *Springer Edit.* (ISBN: 978-981-10-4118-1)
- [15] Antoni J and El Badaoui M 2011, The Random Decrement Technique applied to discrete-time structural vibration signals: closed-form solutions for the blind identification of modal parameters, *Int. Conf. on Structural System Id.*
- [16] Brincker R, Zhang L and Anderser P 2001, Modal identification of output-only systems using frequency domain decomposition, *Smart Materials and Structures* **10** 441-45 (DOI: 10.1088/0964-1726/10/3/303)
- [17] Sadhu A, Narasimhan S and Antoni J 2017, A review of output-only structural mode identification literature employing blind source separation methods, *Mechanical Systems and Signal Processing* **95** 415-31 (DOI: 10.1016/j.ymsp.2017.03.001)
- [18] Poulimenos A-G and Fassois S-D 2006, Parametric time-domain methods for non-stationary random vibration modelling and analysis : A critical survey and comparison, *Mechanical Systems and Signal Processing* **20** 764-816 (DOI: 10.1016/j.ymsp.2005.10.003)
- [19] Ljung L 1999, System Identification, *Prentice Hall* (ISBN: 978-0136566953)
- [20] Brincker R and Ventura C-E 2015, Introduction to Operational Modal Analysis, *Wiley Edit.* (ISBN: 978-1-119-96315-8)
- [21] Peeters B, Van der Auweraer H, Guillaume P and Leuridan J 2004, The PolyMAX frequency-domain method: a new standard for modal parameter estimation?, *Journal of Shock and Vibration* **11** 395-409 (DOI: 10.1155/2004/523692)
- 567 [22] Yuen K-V 2010, Bayesian methods for Structural Dynamics and Civil Engineering, *Wiley Edit.* (ISBN: 9780470824542)
- [23] Pintelon R, Guillaume P and Schoukens J 2007, Uncertainty calculation in (operational) modal analysis, *Mechanical Systems and Signal Processing* **21** 2359-73 (DOI: 10.1016/j.ymsp.2006.11.007)
- [24] Jian F and Yanping Z 2017, Non-stationary random response analysis of structures with uncertain parameters, *Probabilistic Engineering Mechanics* **50** 53-63 (DOI: 10.1016/j.probenmech.2017.10.008)
- 568 [25] Reynders E, Maes K, Lombaert G and De Roeck G 2016, Uncertainty quantification in operational modal analysis with
569 stochastic subspace identification: Validation and applications, *Mechanical Systems and Signal Processing* **66-67** 13-30
570 (DOI: 10.1016/j.ymsp.2015.04.018)
- [26] Reynders E, Pintelon R and De Roeck G 2008, Uncertainty bounds of modal parameters obtained from stochastic subspace identification, *Mechanical Systems and Signal Processing* **22** 948-69 (DOI: 10.1016/j.ymsp.2007.10.009)
- 571 [27] Vu V-H and Thomas M 2014, Uncertainties of Modal Parameters by Operational Modal Analysis, *Mechanics and
572 Industry* **15** 153-58 (DOI: 10.1051/meca/2014018)
- [28] El-Kafafy M, Guillaume P, Peeters B and Coppotelli G 2012, Advanced Frequency-domain Modal Analysis for dealing with measurement noise and parameter uncertainty, *Topics on Modal An.* **5** 179-99 (DOI: 10.1007/978-1-4614-2425-3_17)
- 573 [29] Peeters B, El-Kafafy M and Guillaume P 2012, Dealing with uncertainty in frequency-domain operational modal
574 analysis, *Proc. of the 11th Int. Conf. on Comp. Structures Techno.* (DOI: 10.4203/ccp.99.105)
- 575 [30] Amador S, El-Kafafy M, Cunha Á and Brincker R 2019, A new maximum likelihood estimator formulated in pole-
576 residue modal model, *Applied Sciences* **9** (DOI 10.3390/app9153120)
- [31] Janssens K, Kollar Z, Peeters B, Pauwels S and Van der Auweraer H 2006, Order-based resonance identification using operational PolyMAX, *ResearchGate Source*
- [32] Di Lorenzo E, Manzato S, Dabizzi A, Peeters B, Marulo F and Desmet W 2016, Industrial applications of advanced modal identification on operational rotating machineries, *Proc. of ISMA* 2833-48 (ISBN: 9789073802940)
- [33] Di Lorenzo E, Palermo A, Manzato S, Dabizzi A, Peeters B, Desmet W and Marulo F 2016, Gear Dynamics Characterization by Using Order-Based Modal Analysis, *Proc. of the Int. Modal Analysis Conf.* 387-404 (DOI: 10.1007/978-3-319-30084-9_36)
- [34] Leonard F 2007, Phase spectrogram and frequency spectrogram as new diagnostic tools, *Mechanical Systems and Signal Processing* **21** 125-37 (DOI: 10.1016/j.ymsp.2005.08.011)
- [35] Moisan E, Giacobbi D-B, Gagnon M and Leonard F 2014, Self-excitation in Francis runner during load rejection, *IOP Conf. Ser.: Earth Environ. Sci.* **22** (DOI: 10.1088/1755-1315/22/3/032025)
- [36] Dorfler P, Sick M and Coutu A 2012, Flow-Induced Pulsation and Vibration in Hydroelectric Machinery, *Springer Edit.* (ISBN: 978-1-4471-4252-2)
- [37] Pastor M, Binda M and Harcarik T 2012, Modal Assurance Criterion, *Procedia Engineering* **48** 543-48 (DOI: 10.1016/j.proeng.2012.09.551)

- [38] Yuen K-V and Katafygiosis L-S 2003, Bayesian fast Fourier transform approach for modal updating using ambient data, *Advances in Structural Engineering* **6** 81-95 (DOI: 10.1260/136943303769013183)
- [39] Au S-K 2011, Fast Bayesian FFT Method for Ambient Modal Identification with Separated Modes, *Journal of Engineering Mechanics* **137** 214-26 (DOI: 10.1061/(ASCE)EM.1943-7889.0000213)
- [40] Markert L and Seidler M 2001, Analytically based estimation of the maximum amplitude during passage through resonance, *Int. Journal of Solids and Structures* **388** 1975-92 (DOI: 10.1016/S0020-7683(00)00147-5)
- [41] Tanaka H 2011, Vibration Behavior and Dynamic Stress of Runners of Very High Head Reversible Pump-turbines, *Int. Journal of Fluid Machinery and Systems* **4** 289-306 (DOI: 10.5293/IJFMS.2011.4.2.289)
- [42] Wildheim J 1981, Excitation of rotating circumferentially periodic structures, *Journal of Sound and Vibration* **75** (DOI: 10.1016/0022-460X(81)90386-2)

A Appendix: Theoretical SDoF PSD formulation

As a reminder, the general PSD formulation is given by eq. (1):

$$\mathbf{G}_k = \mathbf{H}_k^* \mathbf{E}_k \mathbf{H}_k^T + \mathbf{A}_k, \quad k \in \llbracket 1, N_f \rrbracket$$

If the excitation is a white noise with equal channel intensities, then the input PSD reduces to a constant matrix \mathbf{E} , independent of the frequency. Moreover, the frequency response function matrix for an SDoF merely reads as:

$$\mathbf{H}_k = D_k^{1/2} \boldsymbol{\varphi} \langle \mathbf{p} \rangle^T \quad (10)$$

where $\boldsymbol{\varphi}$ is the mode shape and $\langle \mathbf{p} \rangle$ is the modal participation factor. Then, eq. (1) can be written as:

$$\mathbf{G}_k = D_k \boldsymbol{\varphi} \langle \mathbf{p} \rangle^H \mathbf{E} \langle \mathbf{p} \rangle \boldsymbol{\varphi}^T \quad (11)$$

Without further development, it appears that $\langle \mathbf{p} \rangle^H \mathbf{E} \langle \mathbf{p} \rangle$ is a scalar independent of the frequency. Defining the scaled modal force as $S = \langle \mathbf{p} \rangle^H \mathbf{E} \langle \mathbf{p} \rangle$, and assuming \mathbf{A}_k to be constant diagonal (i.i.d white channel noise under homoscedastic assumption), then:

$$\mathbf{G}_k = S D_k \boldsymbol{\varphi} \boldsymbol{\varphi}^T + S_e \mathbf{I}_{N_S}, \quad k \in \llbracket 1, N_f \rrbracket \quad (12)$$

which is eq. (2).